Farid *et al. Energy Mater* 2024;4:400041
**DOI:** 10.20517/energymater.2023.96

**Energy Materials**

**Article**

**Open Access**

Check for updates

# Layer-by-layer assembling redox wood electrodes for efficient energy storage

**Tanveer Farid[1,2,3], Yiyun Wang[2], Aamir Razaq[4], Saghir Hussain[5], Weihua Tang[1,2,*]**

[1]The Institute of Flexible Electronics (IFE, Future Technologies), College of Materials, Innovation Laboratory for Sciences and Technologies of Energy Materials of Fujian Province, Xiamen University, Xiamen 361005, Fujian, China.
[2]School of Chemical Engineering, Nanjing University of Science and Technology, Nanjing 20094, Jiangsu, China.
[3]Faculty of Materials Science, Shenzhen MSU-BIT University, Shenzhen 518115, Guangdong, China.
[4]Department of Physics, COMSATS University Islamabad, Lahore Campus, Lahore 54000, Pakistan.
[5]Institute of Chemical Sciences, Bahauddin Zakariya University, Multan 60800, Pakistan.

***Correspondence to:** Prof. Weihua Tang, The Institute of Flexible Electronics (IFE, Future Technologies), College of Materials, Innovation Laboratory for Sciences and Technologies of Energy Materials of Fujian Province, Xiamen University, Xiamen 361005, Fujian, China; School of Chemical Engineering, Nanjing University of Science and Technology, Nanjing 210094, Jiangsu, China. E-mail: whtang@xmu.edu.cn

**How to cite this article:** Farid T, Wang Y, Razaq A, Hussain S, Tang W. Layer-by-layer assembling redox wood electrodes for efficient energy storage. *Energy Mater* 2024;4:400041. https://dx.doi.org/10.20517/energymater.2023.96

**Received:** 7 Dec 2023 **First Decision:** 20 Feb 2024 **Revised:** 28 Mar 2024 **Accepted:** 22 Apr 2024 **Published:** 8 May 2024

**Academic Editors:** Yizhong Huang, Mohamed Gamal Mohamed **Copy Editor:** Fangyuan Liu **Production Editor:** Fangyuan Liu

## Abstract

The exploration of redox-active organic materials and low tortuous thick-electrodes is attractive for energy storage. The *in-situ* valorized lignin on raw wood surface accompanied by layer-by-layer deposition of electro-active materials endow such spatially distributed wood electrodes with high specific capacitance. Here, we report a layer-by-layer assembled ca.1.5 mm-thick redox wood hybrid electrode with 20 mg $cm^{-2}$ electro-active mass loading for efficient energy storage. The *in-situ* modified surface lignin in treated wood (TrW) holds promise as redox-active material with enriched nanoporosity, carbonyl functionalities, and multi-phase ionic transport structure. The carbon nanotubes (CNTs) networking with *in-situ* polymerized polypyrrole (PPy) nanorods three-dimensionally in the lumen of TrW afford a wool-like, highly porous nanostructure. Such a hierarchical structured PPy@CNTs@TrW electrode offers a high areal capacitance of 1.46 F $cm^{-2}$ with an extraordinary energy density of 0.983 mWh $cm^{-3}$ (3.68 Wh $kg^{-1}$) and power density of 5.4 mW $cm^{-3}$ (20.25 W $kg^{-1}$). Here, the valorized surface lignin contributes to electrochemical energy storage accompanied by spatially distributed PPy@CNTs in low tortuous electrodes. The electrode offers extremely low electrochemical impedance of 0.61 Ω electrode resistance and 1.57 Ω electrolyte resistance. The hybrid wood electrode showcases even higher conductivity and energy/ power density than thin carbonized wood and other state-of-the-art thin electrodes made of highly conductive three-dimensional networks. This work highlights the potential of *in-situ* valorized lignin in developing

high-performanceeco-friendly thick-electrodes for electrochemical energy storage applications.

**Keywords:** Redox-active wood, proton storage, lignin valorization, thick-electrode, organic redox supercapacitor, low tortuosity

## INTRODUCTION

The ever-developing market of wearable electronics, electric vehicles, and artificial intelligence has encouraged research on large-scale electrochemical energy storage (EES) devices. EES devices are facing growing demands for high energy density, fast energy storage, extended cyclic life, environment friendliness, and affordability[1,2]. Considerable research efforts have been made to modulate the crystalline structure and morphology of advanced electrode materials for high-performance EES devices over the past years[3-5]. Unique morphologies of nanomaterials have revealed extraordinary chemical and physical characteristics, dramatically different from their corresponding bulk components. Nanostructured electrode materials store a hefty amount of energy and charge/discharge faster if the electrode is thin and loaded with a small active mass[6]. However, the scaled-up hybrid nano-electrodes with high mass loading offer sluggish charge transport kinetics, low energy/power density, and poor structural/chemical stability - limiting their commercial applications. In most cases, an increase in the electrode thickness (ca., ≈100 μm) results in slower kinetics with hindered ion diffusions[7] and thus increased impedance and low energy storage performance[8]. This occurs due to the restricted availability of electrolyte ions to active sites and impeded electron transport inside a fractured structure[9]. Nowadays, these challenges are partially solved by designing three-dimensional (3D) electrodes featuring low tortuosity, fast electron transport structure, and high mass loading capability. The thick-electrode designs are attractive due to their high surface area, fast ion/electron transport and profligate electrochemical reactions offered by nanocrystalline subunits embedded into the highly porous scaffold. Such design also addresses some battery problems, i.e., the hierarchical porous structures accommodate large volume changes during charge/discharge to create stable and durable electrodes.

Natural selection, over billions of years, has endowed organisms with the ability to conduct efficient and optimal metabolic reactions that are impossible for artificial technology to match. Importantly, their energy transduction mechanisms are based on earth-abundant and eco-friendly elements. The “reverse engineering” of these biological entities (ca., important molecules, their products, or even themselves) provides good inspiration for developing next-generation EES devices[10]. For the metabolism, the energy transport from one complex to another in organisms is analogous to electrochemical reactions of EES devices where electrons and ions transport between two electrodes during the charge/discharge process. Such intrinsic redox reactions of organic molecules can also carry out energy transductions in EES devices[11-13]. Some studies have taken advantage of redox-active natural materials to design new electrodes, e.g., biomolecules extracted from biological sources used as active redox materials for EES with high gravimetric energy density[14-16]. Furthermore, their molecular structure is tunable to optimize redox activity and provides large potential for functionalization with other electrochemically active components. Unfortunately, the extraction and processing of redox-active molecules are time- and energy-consuming and require excess chemical utilization[17]. Researchers are keen to explore natural materials in their original form via in-situ modifications to make bioactive molecules environment-friendly and cost-effective. Natural wood (NW) possesses a hierarchical structure composed of aligned cellulose fibers embedded in the matrix of hemicellulose and redox-active lignin. The well-aligned microchannels, micro/nanopores and cellulose nanofibrils in wood offer non-competitive multi-phase transportation for liquids and gases[18]. Especially, the large hierarchical pores with charged surfaces and a swelled polymer matrix offer efficient ionic transference when filled with aqueous or gel electrolytes. The interconnected nanopores open in wide

lumina, making wood an ideal low tortuous scaffold. Most importantly, the lignin contains redox-active molecules potentially beneficial in energy storage after slightly modifying the wood's surface.

In this work, we herein report the facile preparation of redox wood and its further layer-by-layer deposition of carbon nanotubes (CNTs) and polypyrrole (PPy) to generate hybrid electrodes for energy storage in supercapacitors. The chemical treatment on raw wood not only enhances the specific surface area by generating extra nanopores but unlocks molecular chains of lignin to enhance the redox-activity and functionalizability of treated wood (TrW). The CNTs were deposited on wood via sonochemical reaction to generate redox and conductive CNTs@TrW composite. Moreover, PPy nanorods growing *in-situ* on wood surfaces and inside channels afford high mass loading in thick-electrode design. The hierarchically interconnected pores opening in wide lumen provide low tortuosity electrolyte transport pathways [Figure 1].

The as-prepared ultra-thick wood electrode exhibited a high areal capacitance of 1.46 F $cm^{-2}$, an extraordinary energy density of 0.983 mWh $cm^{-3}$ (3.68 Wh $kg^{-1}$), and a remarkable power density of 5.4 mW $cm^{-3}$ (20.25 W $kg^{-1}$), even higher than those for the state-of-the-art thin carbonized wood electrodes. As the delignified wood expands and contracts during a cycling process, the hybrid structure remains intact without any peeling off of PPy to ensure outstanding cycling stability of electrodes. Overall, the redox-active wood-based thick-electrode outperformed many thick-electrodes, opening a new avenue to explore such electrode design further.

## EXPERIMENTAL SECTION

### Materials and reagents

The balsa wood was purchased from a vendor at a local market in Pakistan. The ultra-dry dimethylformamide (DMF) with ≥ 99.8% purity, 4-dimethyl aminopyridine (DMAP) with ≥ 99.0% purity, pyrrole monomer with ≥ 97.0% purity, and $FeCl_3$ catalyst (≥ 95.0% purity) were procured from Merck. Additionally, from Sigma Aldrich, we purchased non-carboxylated multi-walled CNTs with specifications of 6-9 nm diameter and 5 μm length (≥ 95% purity), NaOH (≥ 99.9% purity), $Na_2SO_3$ (≥ 98.0% purity), $HNO_3$ (≥ 90.0% purity), and $H_2SO_4$ (≥ 95.0% purity). None of the compounds underwent extra purification before use.

### Experimental procedure

*Preparation of TrW, CNTs@TrW, and PPy@CNTs@TrW*

The NW samples were boiled at 95 °C in a 150 mL solution of NaOH (2.5 M) and $Na_2SO_3$ (0.5 M) for 1.5 h for delignification. The samples were carefully washed with deionized (DI) water and ethanol and then frozen in a refrigerator for 30 min before being freeze-dried overnight to obtain TrW substrates. The CNTs were first functionalized in a round bottom flask by acidic treatment with $HNO_3$ and $H_2SO_4$ (60:10 ml) for 48 h at 120 °C followed by careful washing with DI water and drying for 24 h at room temperature. The carboxylated CNTs were then dispersed into 50 mL of DMF at a concentration of 2 mg/mL by 1 h ultrasonication to obtain a well-dispersed CNT suspension. For the deposition of CNTs on TrW substrates, the samples were immersed into this suspension followed by the addition of a DMAP cross-linker. The reaction mixture was degassed and ultra-sonicated for 4 h to obtain CNTs@TrW electrodes. The procedure was repeated five times to obtain optimal CNT deposition on the TrW substrate, with wood samples being freeze-dried after each run. For the deposition of PPy on TrW and CNTs@TrW, the samples were further dipped into HCl solution (0.1 M, 80 mL) and degassed for 10 min followed by addition of pyrrole (2 g) monomer. The reaction mixture was cooled to 4 °C in an ice bath followed by the slow addition of catalyst $FeCl_3$ (0.49 g) in aqueous solution (60 mL). After 12 h of polymerization, PPy@TrW and PPy@CNTs@TrW

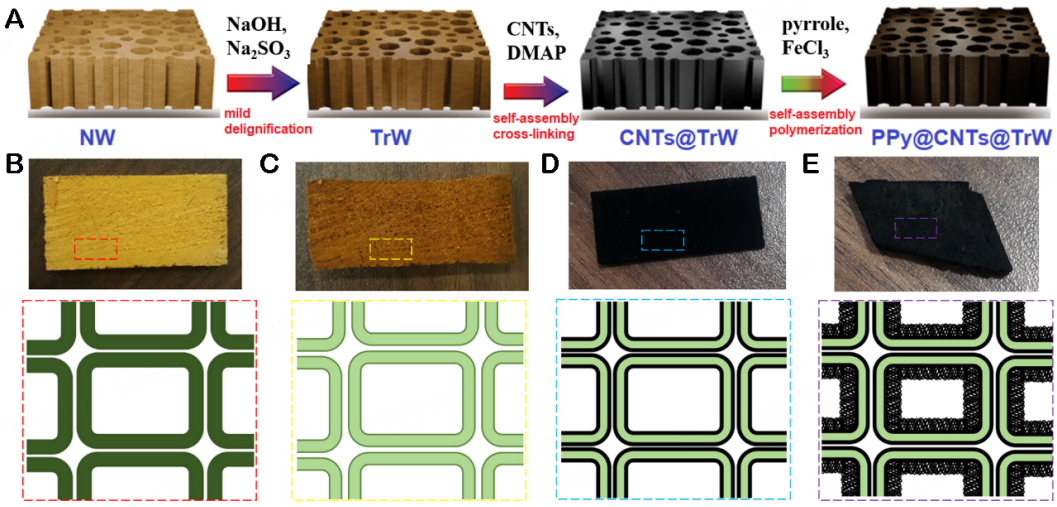


**Figure 1.** (A) Mild delignification and layer-by-layer construction of hybrid wood composites. Optical images of the corresponding samples and the schematic illustration of morphology evolution inside wood cell walls. (B) NW, (C) TrW, (D) CNTs@TrW, (E) PPy@CNTs@TrW.

electrodes were collected by repeatedly washing with 0.1 M HCl, DI water and ethanol before being dried overnight at 60 °C in an oven.

### Characterization

The scanning electron microscopy (SEM) analysis of the sample morphology was performed using a TESCAN/SOLARIS GMH instrument. The transmission electron microscopy (TEM) images were observed using JEOL JEM-F200 at 200 kV. The TEM samples were prepared on copper mesh by scratching powder from electrode surfaces. The X-ray diffraction (XRD) patterns were recorded using Cu Kα radiation ($\lambda \approx 1.54$ Å) on a Bruker D8 Advance diffractometer at 40 kV and 30 mA. The $CO_2$ adsorption-desorption tests were conducted on Micromeritics ASAP 2020, where density functional theory (DFT) methods were used to determine pore size distribution. Concurrently, Brunauer-Emmet-Teller (BET) analysis was applied to calculate the surface area. A Bomen MB154S Fourier Transform Infrared (FTIR) spectrometer was used to collect the FTIR data. The X-ray photoelectron spectroscopy (XPS) was performed on a Thermo ESCALAB 250 X-ray spectrometer (1,486.7 eV) using an Al K radiation source.

The CHI 760D electrochemical workstation was used for the electrochemical measurements. The electrochemical performance was evaluated in a three-electrode system in 1 M $H_2SO_4$ electrolyte, where PPy@CNTs@TrW (or CNTs@TrW, PPy@TrW) was employed as the working electrode, platinum sheet as the counter electrode, and Ag/AgCl as the reference electrode. The areal specific capacitance of electrodes is computed as

$$C_A = \frac{I \times \Delta t}{A \times \Delta V}$$

Or

$$C_A = \frac{\int_{Vc}^{Va} I \times dV}{A \times S \times \Delta V}$$

where $I$, $\Delta t$, $\Delta V$, $A$, $S$, and $dV$ are current, discharge time, electrode area, scan rate and potential window, respectively.

The energy density ($E$) and power density ($P$) of electrodes are calculated as

$$E = \frac{1}{2} \times C_A \times \Delta V^2, \; P = E/\Delta t$$

where $C_A$, $\Delta t$, and $\Delta V$ are areal-specific capacitance, discharge time and voltage, respectively.

## RESULTS AND DISCUSSIONS

### Wood modification and characterization

The cellulose fibers of wood are naturally arranged in the polymer matrix of lignin and hemicellulose to form a highly hierarchical porous structure. The porosity of wood comes from the systematic assembly of nanoscale constituents, which arrange themselves in a way to prepare tube-shaped vessels, tracheids, and fibers[19]. These tube-shaped structures are further embedded with micro to macroscale porosity in the form of pits and nanopores within the lignin matrix. This hierarchical porosity is naturally designed in wood to support the transport of nutrients, water and ions in the entire tree. Here, we performed a mild delignification to remove part of lignin and hemicellulose from cell walls and middle lamella by boiling NW samples in $NaOH/Na_2SO_3$ solution for 1 h. The chemical treatment removed plenty of lignin and hemicellulose, leaving voids in the polymer matrix and lignin structure via cleavage of C-O bonds. The rest of the lignin matrix was left intact with some of the opened molecular structure of the polymer matrix and cellulose. The TrW was freeze-dried in the presence of $NaOH/Na_2SO_3$ to preserve porosity. The drying process helped to reassemble the lignin matrix through hydrogen bonding, and the presence of $NaOH/Na_2SO_3$ crystals facilitated porosity preservation.

The SEM images reveal the difference in the surface roughness before and after the delignification of wood samples. Upon closer inspection of the NW images, it is clear that the interior of the cell wall is completely smooth [Figure 2A-D]. At the same time, the roughness in the cell walls of TrW samples is visible in SEM images. The smoothness of the NW surface is due to uniform surface coverage by the lignin matrix and residual nutrients/wax left over the cell wall surfaces. The TrW images show exposed nanostructure inside the lumina, and the cell wall surface gives a rough and bumpy appearance [Figure 2E-H]. The natural 3D honeycomb structure of NW was unaffected by the mild delignification, while removing lignin/wax created the nanoscale pores. On the other hand, EDS analysis reveals about 17% decrease in C atoms (based on C, O, N, S, Na, and Fe being 100% cumulatively) due to lignin and hemicellulose removal after delignification [Figure 2I-L]. Furthermore, the atomic percentage of O increased by about 1.6% even after delignification - suggesting an increase in oxygen-containing functionalities after cleavage of C-O bonds in TrW samples. As expected, a minor deposition of Na and S elements and decrease in Fe atoms were also observed in TrW samples. After partial delignification and careful drying, the NW transformed into a highly porous and carboxy-and hydroxy-enriched TrW scaffold, suitable for EES in lignin structure and further functionalization.

The effect of chemical treatment on specific surface area and porosity was quantified through adsorption-desorption isotherms of $CO_2$. Both factors affect the functionalizability of the wood scaffold and microfluidic transport characteristics, wherein improved specific surface area and porosity are favorable. All

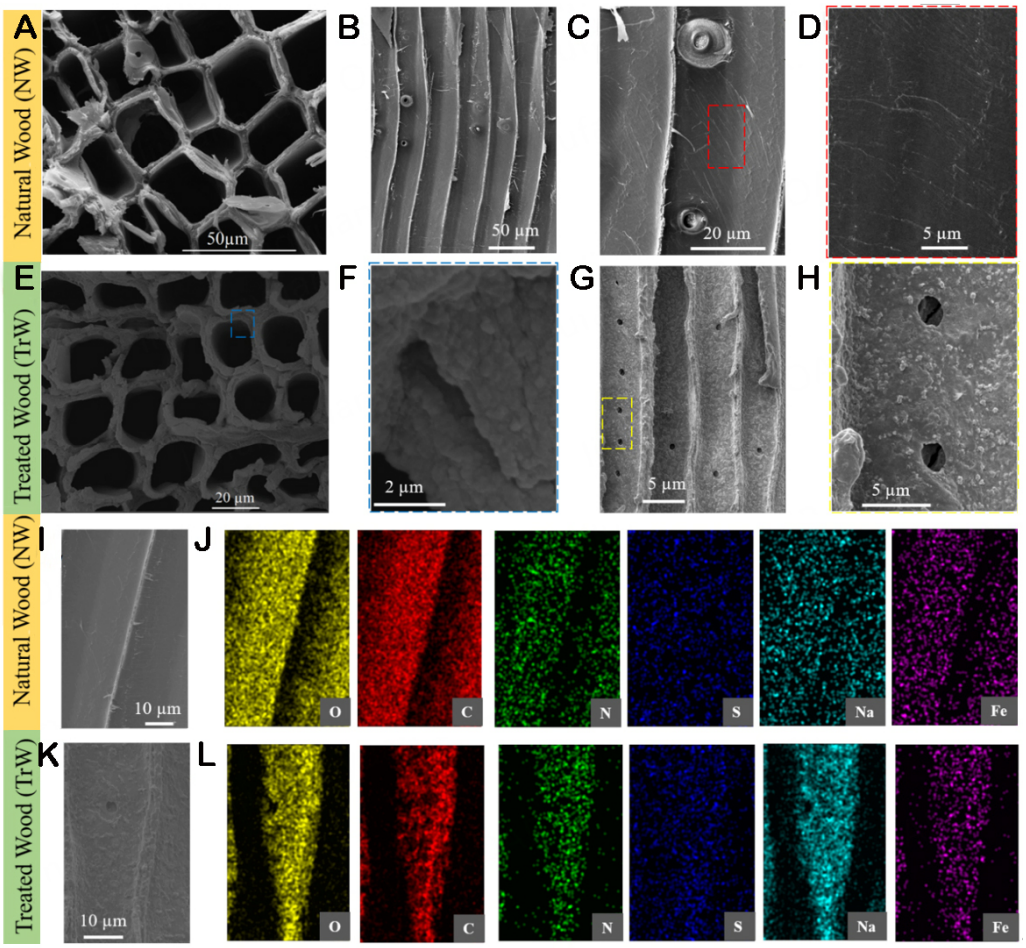


**Figure 2.** The microstructural analysis and elemental mapping of NW and TrW through SEM and EDS. (A) Top-view SEM image of NW showing open large pores - beneficial for cell wall surface modification and layer-by-layer assembly of nanomaterials, (B-D) Side-view SEM images of NW cell wall surface from low to high resolution showing vertical channels and smooth cell wall surface. (E and F) Followed by the top-view SEM images of TrW showing decrease in channel width and modified lignin at the surface. (G and H) Side-view SEM images of TrW with modified lignin at cell wall surface. (I and J) EDS elemental maps of NW showing Oxygen (O), Carbon (C), and Nitrogen (N) as major components and Sulfur (S), Sodium (Na), and Iron (Fe) as minor constituents of NW. (K and L) EDS elemental maps of TrW showing O, C, and N as major components and S, Na, and Fe as minor constituents of TrW.

the adsorption-desorption isotherms [Supplementary Figure 1A and B] showed typical type IIB behavior wherein micropores filled at low relative pressure ($P/P_o$ = 0-0.2)[20]. Remarkable mesoporous adsorption was evidenced by continuous adsorption in the intermediate relative pressure range. The steep adsorption in a high relative pressure range indicates exceptional adsorption by macropores of treated and untreated NW. The freeze-dried TrW samples showed enhanced adsorption in the micro and mesoporous region [Supplementary Figure 1C and D], and a characteristic sharp step-down in the desorption curve is called "cavitation" - a sign of a significant level of micro- and mesoporosity[21,22]. All samples showed H4-type hysteresis loops with non-limiting adsorption at high relative pressure[23]. The distribution of loops over a wide relative pressure range proves the presence of pores with varied diameters in wood. Such hysteresis loops are observed in natural materials and signify aggregation of slit-shaped pores organized hierarchically. It has already been evidenced that delignification creates microporosity in the lignin matrix[24,25]. The specific BET measurements reveal the surface area as 44.65 and 54.83 $m^2 g^{-1}$ for NW and TrW, while the average pore diameters are 7.97 and 6.08 nm for NW and TrW, respectively [Supplementary Table 1].

The chemical surface modification of wood was also evaluated with FTIR and XPS. Bands of Most NW become more apparent after the wax is removed by chemical treatment. The results suggest a slight modification in the wood surface with mainly preserved wood components [Supplementary Figure 1E and F]. Remarkably increased intensities are observed for bands 3,340 and 1,036 $cm^{-1}$ assigned to O-H stretching and vibration, respectively[26]. A considerable decrease in the hemicellulose-related band is observed at 1,734 $cm^{-1}$ (C=O unconjugated stretching) for TrW samples[27]. The band at 1,234 $cm^{-1}$ (C-O stretching and C-H plane vibration) with decreased intensity red-shifts and separates into multiple peaks (mainly at 1,268, 1,224, and 1,200 $cm^{-1}$), suggesting the chemical modification in guaiacyl and syringyl lignin. Increase intensities are also found for cellulose- and lignin-related bands, including 897 $cm^{-1}$ (C-H rocking vibration), 1,503 $cm^{-1}$ (C=C stretching of lignin), and 1,592 $cm^{-1}$ (C=O stretching of lignin), and 2,890 $cm^{-1}$ (C-H stretching)[28,29]. The C-H/C-O vibrations of cellulose- and syringyl lignin-related bands increase and shift from 1,326 $cm^{-1}$ in NW to 1,315 $cm^{-1}$ in TrW[27,30]. New bands (1,743 and 1,625 $cm^{-1}$) observed for CNTs@TrW are attributed to C=C stretching from functionalized CNTs[31]. The band at 1,592 $cm^{-1}$ in TrW related to C=O stretching of lignin shifts to 1,576 $cm^{-1}$ in CNTs@TrW, which is attributed to π-π and hydrogen bonding between CNTs and TrW surface[32,33]. The absorbance at 2,890 $cm^{-1}$ is separated into two different peaks at 2,850 and 2,927 $cm^{-1}$ due to the chemical interaction between CNTs and TrW in CNTs@TrW composites.

The mild delignification removal of wax from the wood surface makes the surface functionalities clearer, as indicated by the XPS spectra [Figure 3A and B]. This implies that chemical treatment made the surface lignin dissolve in the form of debris and enriched the material surface, resulting in excess lignin coverage. The NW exhibits the main elements as C (285 eV) and O (532 eV) and a small amount of N (399 eV) from the XPS full survey scan. The O/C ratio can be used to assess the composition of the outer surface of NW, including carbohydrate, lignin and extractive content [Supplementary Table 2]. The O/C ratios of NW and TrW samples remained close to the theoretical values of lignin (0.33), implying that lignin is the outer surface of scaffolds[34]. The surface coverage by lignin in the TrW sample remained 100% despite its total amount being reduced. Based on the carbon atoms in wood, the C1s peak [Figure 3C and D] is deconvoluted into four subpeaks: C1 containing C-C/C-H groups mainly corresponding to lignin; C2 and C3 having C-O/C-OH and C=O/O-C-O based on carbohydrate; C4 referring to O-C=O groups present in carboxylic acids and other substances[34]. The mild delignification decreased the degree of lignin polymerization, increasing the amount of C1 and C4 while decreasing the relative contents of C2 and C3. More phenolic hydroxyl radicals and lignin degradation products are exposed, which can enhance redox activity and functionalization of the TrW scaffold. The O1s peak for TrW is deconvoluted into three subpeaks: O1 containing O-C=O associated with lignin; O2 containing C-O of cellulose and hemicellulose; O3 containing C-OH associated with lignin [Figure 3E][35]. The NW samples only showed O1 and O2 peaks having a slight binding energy difference [Figure 3F]. TrW exhibits an O3 signal of lignin because of wax removal and exposed surface lignin. The relative content of O2 in wood decreased after treatment, indicating the displacement of hemicellulose.

### Lay-by-layer assembling thick-wood hybrid

The highly porous and hydroxy-enriched TrW substrates were ultra-sonicated in carboxylated CNT dispersion in the presence of DMAP. The chemical immobilization of CNTs onto TrW cell walls via esterification was accelerated under the catalysis of DMAP. The freeze-thaw process then dried the samples, and such a two-step procedure was repeated five times. SEM images reveal a well-organized porous CNT network on the cell wall surface [Figure 4A-C]. Several CNTs have arranged themselves into lengthy bundles - clusters of CNTs self-assembled into a conductive network layer. The CNT networks exhibited high mesoporosity with cross-linking manners. The obtained CNTs@TrW electrode thus presents a good hierarchical structure with implanted conductivity, where cell walls with cellulose fibers embedded in lignin

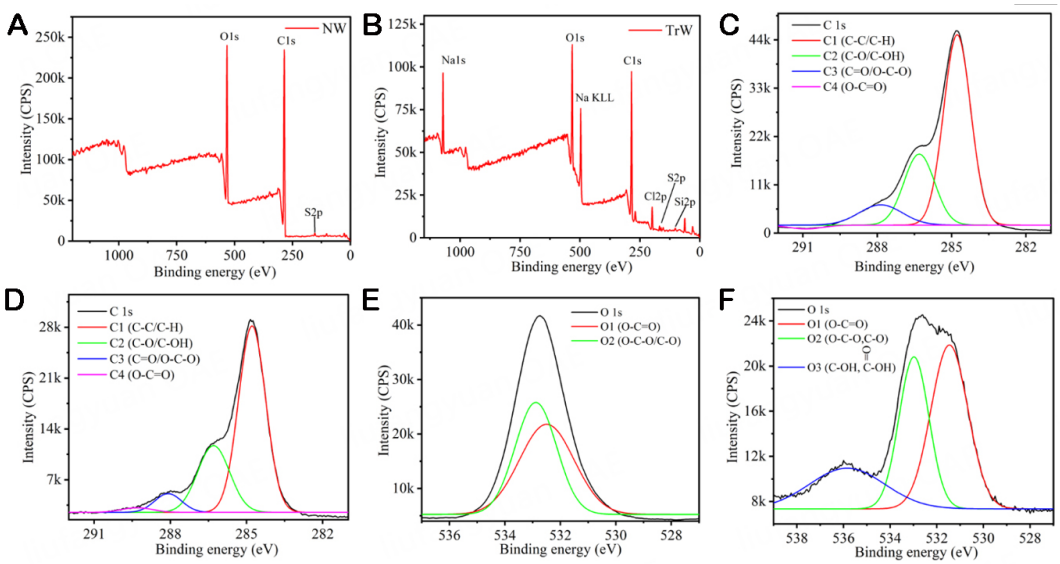


**Figure 3.** XPS survey spectra of (A) NW and (B) TrW. Deconvoluted C1s spectra of (C) NW and (D) TrW. Deconvoluted O1s spectra of (E) NW and (F) TrW.

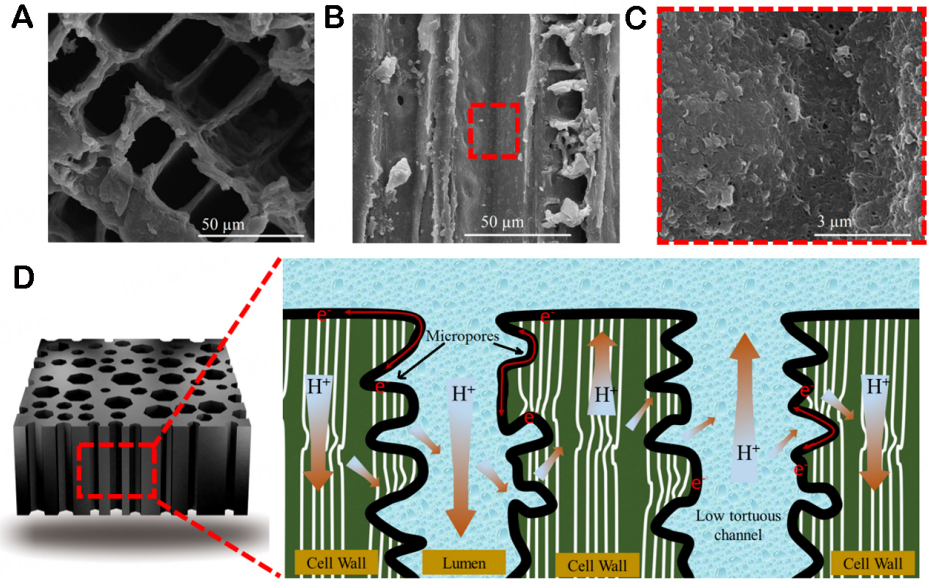


**Figure 4.** (A) Top-view and (B) cross-sectional SEM images of CNTs@TrW. (C) High magnification view of CNTs@TrW cell wall. (D) Schematics of the charge transport mechanism in thick CNTs@TrW hybrid. The cell walls have cellulose fibers embedded in the lignin matrix, where the cell walls can be saturated with electrolytes transported from cellulose fibers. The cell walls are coated with CNTs to enable electron transport. The lumen filled with electrolytes makes low tortuosity channels for transporting ions to neighboring micropores.

matrix are coated with highly conductive layers and hollow tube-shaped lumen channels open for electrolyte transport [Figure 4D]. The conducting layers facilitate redox reactions of surface lignin as a porous interface and pathways for electron transport. The cell walls can be saturated with electrolytes transported by cellulose fibers. Electrolyte-filled lumens accompanied by micropores form low-tortuous channels, forming a multi-phase transport system to efficiently shuttle ions across thick-wood electrodes.

The PPy@CNTs@TrW hybrids were further prepared by *in-situ* redox polymerization of PPy on CNTs@TrW substrate. The slow deposition of PPy on the cell wall surface afforded a wool-like, highly porous structure. The PPy started aggregation around CNTs and spread three-dimensionally to make a highly porous nanostructure [Figure 5A-G]. The intercellular space pores in cell walls and ray cells were partially filled with nanorods. The PPy nanorods are aggregated into nanofibers to form an interconnected fiber mesh in the lumen connecting the cross-section of cell walls. The conductive structure is highly porous at the microscale and resembles soft wool-like composites. At the nanoscale, the well-separated PPy nanorods construct a highly porous structure. For reference, we also prepared PPy@TrW without CNTs by following similar redox polymerization of pyrrole. The resultant binary composite reveals the growth of PPy nanoball on the cell wall surface and lumina to make a full coverage [Figure 5H-M]. Compared to PPy@CNTs@TrW SEM images, less mass loading was observed on cell walls of PPy@TrW, indicating the positive role of CNTs in guiding the self-assembly of pyrrole to polymerize *in-situ* on cell walls.

The TEM and EDS analyses further give insight into structure and composition of PPy and PPy@CNTs deposited over wood surfaces. The PPy, depicted as uniform solid nanoballs with an average of 80 nm in diameter, aggregates at the wood surface to form a conductive coating [Figure 6A-C]. Meanwhile, PPy@CNTs samples show a wool-like nanostructure wrapping around CNTs and extending towards the substrate surface for interfacial coating between wood and CNTs [Figure 6D-F]. The results indicate that the interaction between the CNT surface and PPy during polymerization significantly influenced the wool-like nanostructure formation of PPy, as observed in SEM. In this core-shell structure, the CNTs provide chemical and mechanical stability and excellent conductivity, while porous structure of PPy takes lead in providing active sites for energy storage through high surface area. On the other hand, the EDS analysis shows C as the dominant element followed by N in both structures with O also being part of it - indicating the presence of oxygen functionalities in the structure as well. Here, the presence of Fe is less than 0.07 % in both cases, showing complete washing of the $FeCl_3$ catalyst from the structures.

The deposition of PPy on CNTs@TrW or TrW can be revealed from FTIR analysis [Figure 6G and Supplementary Figure 2]. New high-intensity characteristic peaks for PPy appeared at 1,530/1,552 (C=C stretching), 1,290 (C-H out-of-plane bending), 1,201 and 1,471 (C-N stretching), and 889 $cm^{-1}$ (N-H out-of-plane bending). The peaks at 1,444 and 959 $cm^{-1}$ (O-H bending) show the hydrophilic nature of PPy-deposited hybrids[36-38]. The absorption at 1,712 $cm^{-1}$ in PPy@TrW is assigned to C=O stretching vibration in PPy bulk, indicating non-porous aggregation of PPy on the wood surface[39,40]. The shift from 1,552 to 1,530 $cm^{-1}$ (C=C stretching) indicates the formation of π-π interactions between CNTs and PPy in the PPy@CNTs@TrW nanocomposite[41]. The peak at 2,978 $cm^{-1}$ is attributed to the stretching vibration of the $-CH_2-$ group of the pyrrole ring. After the layer-wise deposition of CNTs and PPy on TrW, most of its characteristic XRD peaks are suppressed, suggesting a full coverage of electro-active mass on these scaffolds [Figure 6H and Supplementery Figure 3]. As shown, TrW demonstrated a strong peak (004) at $2\theta = 34.4°$ with the preserved structure of the wood scaffold. A cumulative hump is observed for TrW, corresponding to cellulose $(11\bar{0})$, $(11\bar{0})$ and (110) planes at $2\theta = 14.8°$, 12.30° and 16.5°. Another hump can be found in TrW composed of peaks at $2\theta = 20.5°$, 21.7° and 22.8° [assigned to (110), (020) and (200) cellulose planes][39]. Both PPy@CNTs@TrW and PPy@TrW composites exhibit only two intensified hump peaks centered at $2\theta = 22.50$ and 15.10°, indicating the deposition of CNTs and PPy along the cellulose-fiber wall.

### Electrochemical performance

The energy storage properties of our TrW-based composites as electrodes were first evaluated in three-electrode electrochemical systems. The cyclic voltammetry (CV) of CNTs@TrW and CNTs@NW electrodes

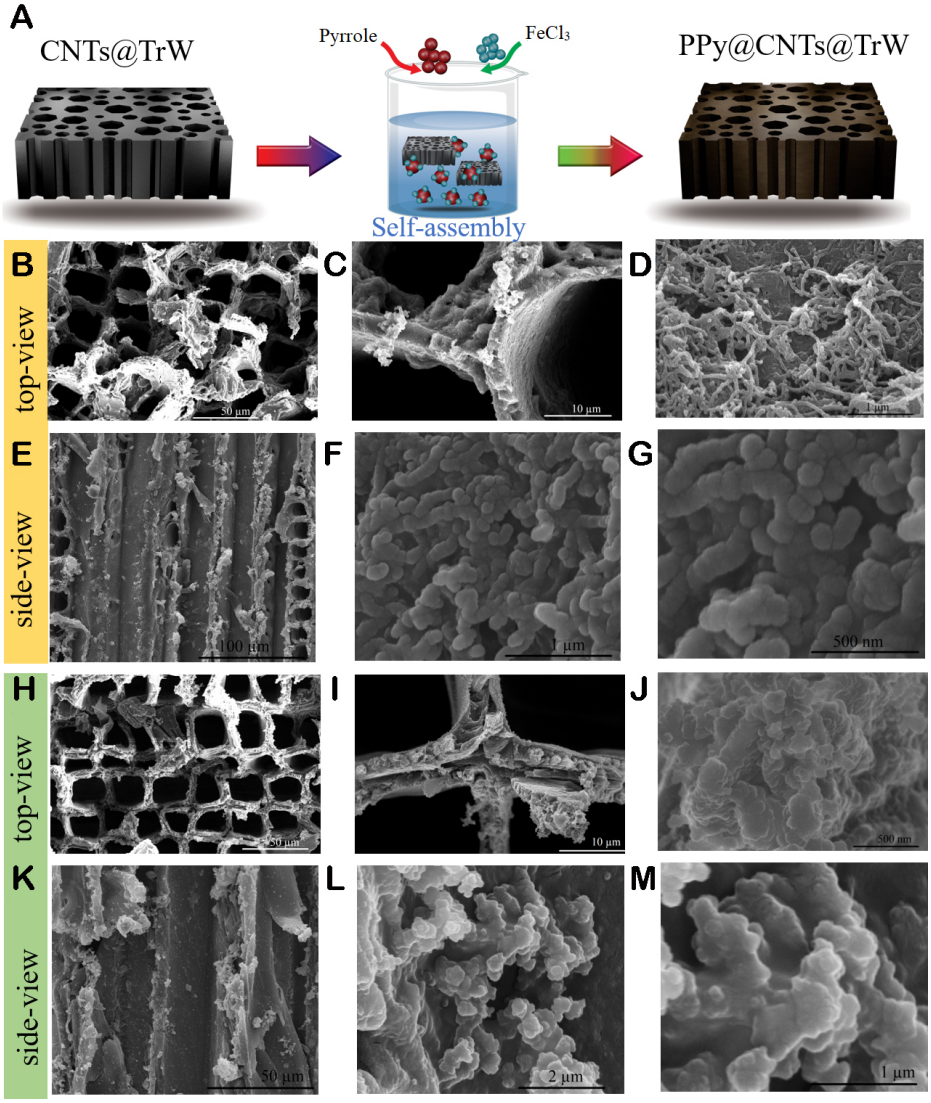


**Figure 5.** (A) *In-situ* redox polymerization of pyrrole on CNTs@TrW. (B-D) Top-view SEM images of PPy@CNTs@TrW at different magnifications, showing uniform PPy coating on CNTs surface. (E-G) side-view SEM images of PPy@CNTs@TrW at different magnifications, showing a high amount of PPy nanorods aggregated on the cell wall surface. (H-J) Top-view and (K-M) side-view SEM images of PPy@TrW showing uniform PPy coating on the wood surface. The images show a limited amount of PPy aggregation on the TrW surface.

exhibit clear deviance from the typical rectangular trace corresponding to CNTs, where a well-defined pair of redox peaks are observed at 0.5 and 0.35 V versus Ag/AgCl, respectively, in 1 M aqueous $H_2SO_4$. The electric double layer capacitor (EDLC) behavior, in combination with the Faradaic reaction, ensures enhanced charge transport [Figure 7A and B]. The faradaic redox reaction can be assigned to the $Q/QH_2$ pair from raw lignin ($QH_2 \rightleftharpoons Q + 2e^- + 2H^+$)[42,43]. This suggests the creation of an electrochemical double layer at the electrode surface and redox reactions at the wood surface. The distinct pair of redox peaks highlights the contribution of carbonyl functional groups containing lignin molecules in overall electrochemical performance of electrodes. The carbonyl groups (-C=O) accept electrons during reduction to transform into hydroxyl groups (-C-OH), while the hydroxyl groups reversibly lose electrons during

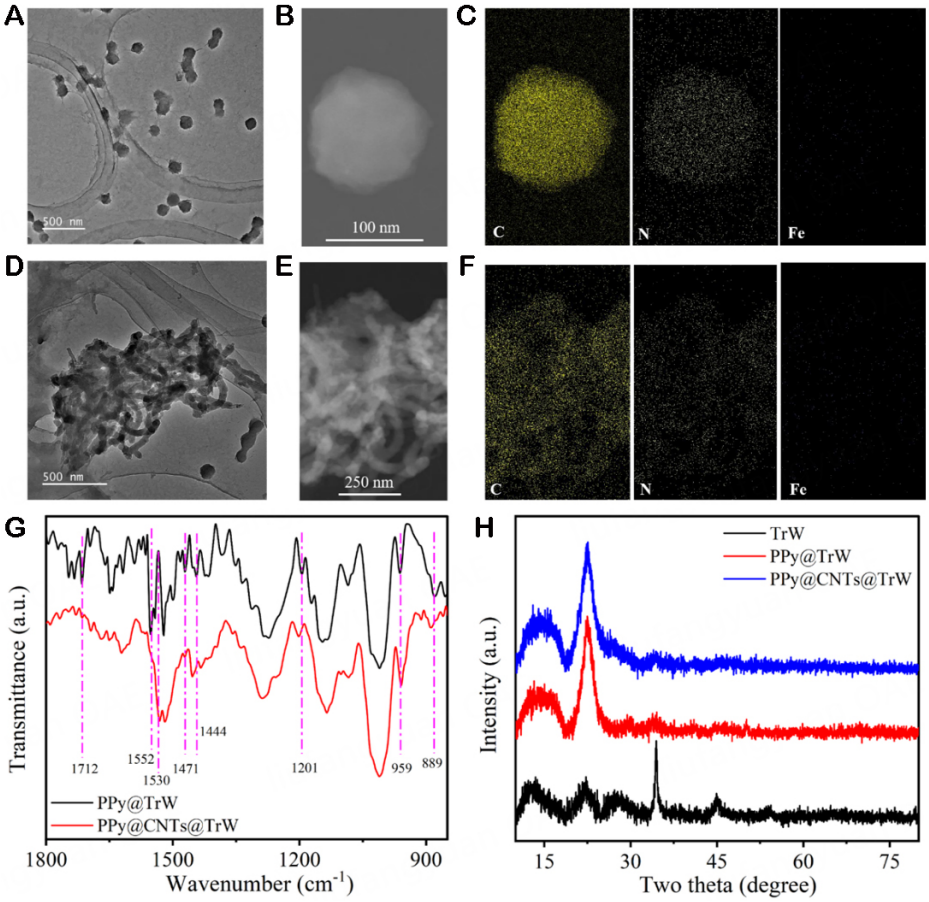


**Figure 6.** (A-C) TEM and EDS analysis of PPy nanostructure, after scratching powder from PPy@TrW electrode. (D-F) TEM and EDS analysis of PPy@CNTs nanostructure, after scratching powder from PPy@CNTs@TrW electrode. (G) FTIR plots in 850-1,800 $cm^{-1}$ region for PPy@TrW and PPy@CNTs@TrW. (H) XRD plots of TrW, PPy@TrW and PPy@CNTs@TrW.

oxidation to revert to carbonyl groups. Thus, presence of carbonyl groups in lignin structure contributes to redox reactions by accepting protons ($H^+$) from acidic electrolyte - contributing to electrode capacitance [Figure 7C][44,45]. Comparably, the CNTs@TrW electrode shows more prominent redox peaks, suggesting the effectiveness of chemical treatment of NW before CNT deposition. Evidence from SEM images and BET analysis indicates that the modified lignin showed increased surface area and nanopores - contributing to increased redox activity in CNTs@TrW electrodes. Furthermore, enhanced carbonyl signals in FTIR and XPS analysis reveal the importance of lignin modification on wood surfaces, significantly affecting the redox activity of CNTs@TrW electrodes.

The galvanostatic charge/discharge (GCD) process was further performed at an increasing current density from 0.4 to 5.0 mA $cm^{-2}$ in the potential window of 0 to 1.0 V [Supplementary Figure 4]. Unlike symmetrical triangle GCD traces observed for most carbon electrodes, the CNTs@TrW electrode exhibits distinct tailing in the discharge process at current densities below 1.0 mA $cm^{-2}$. Similar but smaller tailing GCD traces are found for both CNTs@NW and PPy@TrW electrodes, further confirming the redox behavior of raw lignin [Supplementary Figure 5]. We can calculate the area-specific capacitance ($C_A$, in F $cm^{-2}$) using the discharge time and electrode dimensions. Notably, the CNTs@TrW electrode displayed a high $C_A$ of 136, 123, 118 and 113 mF $cm^{-2}$, corresponding to scan rates of 0.4, 1, 3, and 5 mA $cm^{-2}$. The high-rate capability of CNTs@TrW can be attributed to the hierarchically porous redox structure to promote efficient penetration

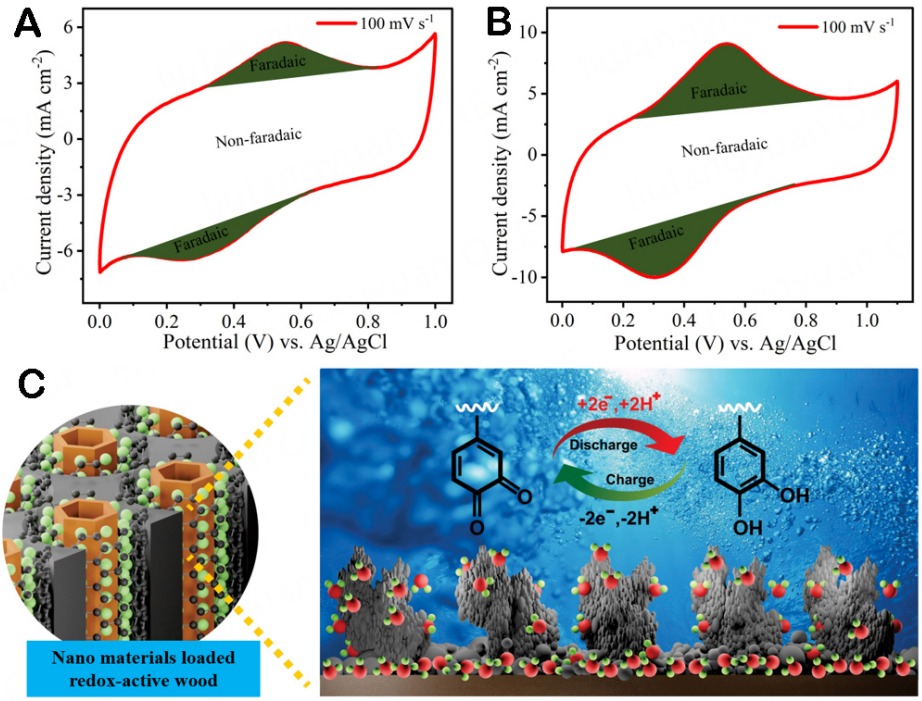


**Figure 7.** (A and B) CV plots of CNTs@NW and CNTs@TrW at 100 mv $s^{-1}$ showing distinct redox peaks. Enhanced redox peaks were observed in CNTs@TrW samples as compared to CNTs@NW. (C) Schematic elaboration of redox reactions supported by redox-active lignin in supercapacitor electrodes.

of electrolytes and the 3D CNT network to ensure fast transfer of electrons. This finding indicates robust integration and stability of CNTs on the TrW surface.

In contrast, PPy@CNTs@TrW thick-electrodes exhibit combined EDLC and pseudocapacitive behavior. The CV curves showed a nearly rectangular behavior in the potential window of -0.1 to 0.8 V at a wide scan rate increasing from 10 to 100 mV $s^{-1}$ [Figure 8A]. The GCD curves of PPy@CNTs@TrW are nearly triangular in current densities ranging from 1 to 50 mA $cm^{-2}$ [Figure 8B]. Significantly, PPy@CNTs@TrW electrodes exhibited high areal capacitance of 1.46, 1.36, 1.067, and 0.61 F $cm^{-2}$ at the current density of 2, 5, 10, and 50 mA $cm^{-2}$, respectively [Figure 8C]. Compared to PPy@TrW, these electrodes showcased 30 times higher capacitance. This improved capacitance indicates the importance of the conductive network between the cell wall and electrochemically active material. The porous CNT networks templated the PPy network to grow in mesh form providing high surface area and ensuring fast charge transport to each active site. Combining a conductive network and spatially distributed nanomaterial makes an ideal design of 3D thick-electrodes.

Let us analyze Nyquist plots by considering electrode ($R_e$), electrolyte ($R_\infty$), and internal resistance ($R_i = R_e + R_\infty$)[46]. For the CNTs@TrW electrode, the electrochemical impedance spectroscopy (EIS) profile displays typical carbon-based EDLC behavior, such as a perfect semicircle at high frequencies, a nonlinear line at intermediate frequencies, and a nearly vertical line at low frequencies [Figure 8D]. The CNTs@TrW electrode had a minute $R_i$ of 1.5 Ω, resulting from a small semicircle width for $R_\infty$ of 1 Ω and a small $R_e$ (0.5 Ω). The superior electrode conductivity reveals the defect-free interconnectivity of CNTs to form a charge transport network. Furthermore, the surplus electrolyte absorbed by micropores beneath the CNT layer provides efficient diffusion of ions all through the conductive layer. When the CNT network was

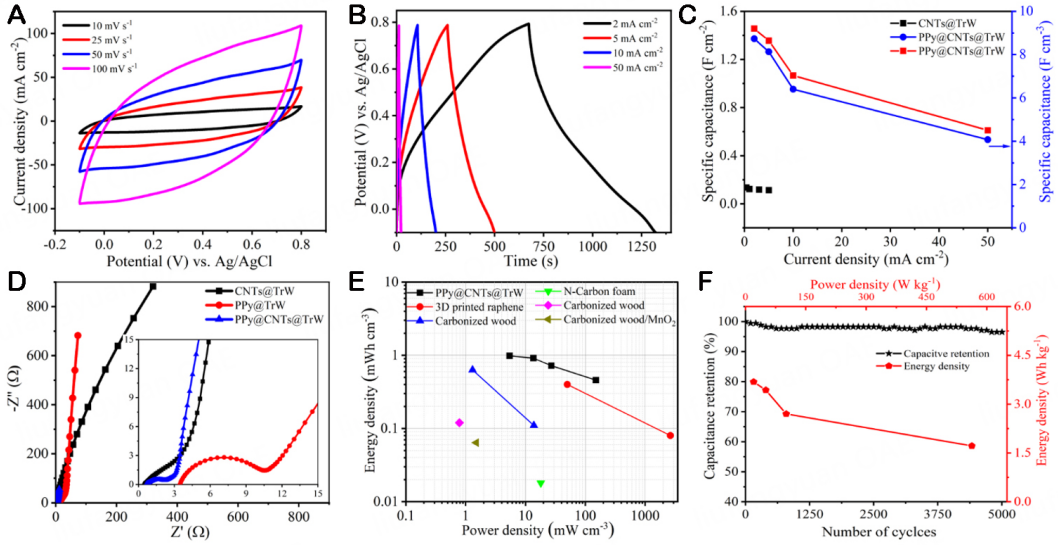


**Figure 8.** Electrochemical profile of PPy@CNTs@TrW thick electrode. (A) CV curves of PPy@CNTs@TrW at scan rate increased from 10 to 100 mV $s^{-1}$.(B) GCD curves of PPy@CNTs@TrW at different current densities. (C) Correlation between areal and volumetric specific capacitance and current density of CNTs@TrW and PPy@CNTs@TrW. (D) EIS profile of CNTs@TrW, PPy@TrW, and PPy@CNTs@TrW having full-scale graph and zoomed one to show semicircle. (E) Ragone plot of our thick PPy@CNTs@TrW electrodes with typical carbon electrodes in the literature. (F) Capacitive retention over charge-discharge cycles and plot of gravimetric energy density against gravimetric power density.

sandwiched between the cell wall and PPy, the PPy@CNTs@TrW electrode exhibited only a small $R_i$ of 2.18 Ω, a sum of a minimal $R_e$ (0.61 Ω) and a small semicircle for $R_\infty$ of 1.57 Ω. The excellent electrode conductivity reveals defect-free interconnectivity of CNTs with PPy to perform effective charge transport. Additionally, the small electrolyte resistance shows that the excess electrolyte absorbed by micropores under the PPy@CNTs layer ensures effective ionic transport throughout the active material. The complete and small semicircle reveals a perfect material electrolyte interface. On the other hand, the PPy@TrW electrode manifested internal resistance $R_i$ of 10.6 Ω. The electrode and electrolyte resistance was calculated as 3.3 and 7.3 Ω, respectively. A sharp decrease of 500% and 550% in overall and electrode resistance in PPy@CNTs@TrW reveals the importance of the CNT layer under PPy nanorods. The high conductivity of our developed PPy@CNTs@TrW makes it a strong competitor of carbonized wood electrodes in the literature, e.g., carbonized wood, $Co(OH)_2$ carbonized wood[47], N and S co-doped wood carbon[48], and activated wood carbon[49]. More importantly, the reported carbonized wood electrodes usually suffer from mechanical failure at even minor stress. In contrast, our PPy@CNTs@TrW electrode is a microporous natural fiber-based scaffold that resists mechanical failure under external stresses and expansions/contractions during charge-discharge.

The PPy@CNTs@TrW electrode delivered a maximum volumetric energy density of 0.983 Wh $cm^{-3}$ (3.68 Wh $kg^{-1}$), 0.915 Wh $cm^{-3}$ (3.43 Wh $kg^{-1}$), 0.720 Wh $cm^{-3}$ (2.7 Wh $kg^{-1}$), and 0.458 Wh $cm^{-3}$ (1.72 Wh $kg^{-1}$) at volumetric power densities of 5.4 mW $cm^{-3}$ (20 mW $kg^{-1}$), 13.5 mW $cm^{-3}$ (50.6 mW $kg^{-1}$), 27 mW $cm^{-3}$ (101 mW $kg^{-1}$), and 150 mW $cm^{-3}$ (563 mW $kg^{-1}$), respectively. In supercapacitors, our electrode delivered higher volumetric energy and power densities than carbonaceous electrodes (ca., carbonized wood, carbon foam, graphene aerogel, *etc.*) [Figure 8E and F][50-54]. As expected, the PPy@CNTs@TrW electrode demonstrates outstanding cycling performance, i.e., over 93% capacitance retention observed after 5,000 GCD cycles indicates strong interconnectivity and stability of functional nanomaterial to the cell wall surface [Figure 8F]. The conducting polymers usually exhibit low cyclic stability because of degradation by

expansion and contraction of material during charging-discharging. In the case of PPy@CNTs@TrW, the cell wall can easily accommodate expansions and contractions of nanomaterials, leading to high cycling stability.

## CONCLUSIONS

In conclusion, we successfully *in-situ* valorized raw lignin of wood scaffold via C-O bond cleavage to use it as a redox-active material in low-tortuous thick-electrode. The electrodes were prepared via simple chemical treatment of raw wood followed by layer-by-layer deposition of electroactive nanomaterials. The chemically treated wood is a one-of-a-kind mesoporous structure with oxygen functionalities in its rich surface lignin and multi-phase ion transport system composed of cell walls running along thickness and micropores running horizontally. The as-prepared electrodes exhibited excellent redox activity in 1M $H_2SO_4$ electrolyte - storing protons in lignin structure. The layer-by-layer assembled PPy@CNTs@TrW. The resulting PPy@CNTs@TrW electrode with a thickness of 1.5 mm and a high mass loading of 20 mg $cm^{-2}$ delivered a high areal capacitance of 1.46 F $cm^{-2}$ in addition to a high volumetric energy and power density of 0.983 and 5.4 mW $cm^{-3}$. These values were significantly higher than those reported for carbon-based thick-electrodes. he low-tortuous redox-active wood holds promise in different research areas, including catalysis, gas separations, membranes, sensors, biomedical, and battery applications.

## DECLARATIONS

### Acknowledgement

We gratefully acknowledge the financial support from the National Natural Science Foundation of China, Tan Kah Kee Innovation Laboratory, and the Key R&D Program of Natural Science Foundation of Jiangsu Province. Tanveer F thanks China Scholarship Council and Nanjing Municipal Government for the Scholarships.

### Authors' contributions

Methodology, investigation, and writing manuscript: Farid T
Project administration and funding acquisition: Tang W
Discussed the whole paper: Razaq A, Hussain S
Performed the measurements: Wang Y
Conceptualization and supervision: Tang W

### Availability of data and materials

The data supporting our work can be found in the Supplementary Materials.

### Financial support and sponsorship

This work is supported by the financial support from the National Natural Science Foundation of China (Grant Nos. 22375170 and 51861145401), Tan Kah Kee Innovation Laboratory (HRTP-[2022]-45), and the Key R&D Program of Natural Science Foundation of Jiangsu Province (BE2019733).

### Conflicts of interest

All authors declared that there are no conflicts of interest.

### Ethical approval and consent to participate

Not applicable.

### Consent for publication

Not applicable.



## REFERENCES

1. Choi C, Ashby DS, Butts DM, et al. Achieving high energy density and high power density with pseudocapacitive materials. *Nat Rev Mater* 2020;5:5-19. DOI
2. Lin J, Zhang X, Fan E, Chen R, Wu F, Li L. Carbon neutrality strategies for sustainable batteries: from structure, recycling, and properties to applications. *Energy Environ Sci* 2023;16:745-91. DOI
3. Gan Z, Yin J, Xu X, Cheng Y, Yu T. Nanostructure and Advanced Energy Storage: Elaborate Material Designs Lead to High-Rate Pseudocapacitive Ion Storage. *ACS Nano* 2022;16:5131-52. DOI
4. Zhang L, Feng R, Wang W, Yu G. Emerging chemistries and molecular designs for flow batteries. *Nat Rev Chem* 2022;6:524-43. DOI
5. Zheng J, Archer LA. Crystallographically textured electrodes for rechargeable batteries: symmetry, fabrication, and characterization. *Chem Rev* 2022;122:14440-70. DOI PubMed
6. Eng AYS, Soni CB, Lum Y, et al. Theory-guided experimental design in battery materials research. *Sci Adv* 2022;8:eabm2422. DOI PubMed PMC
7. Wu F, Liu M, Li Y, et al. High-mass-loading electrodes for advanced secondary batteries and supercapacitors. *Electrochem Energ Rev* 2021;4:382-446. DOI
8. Cheng HM, Li F. Charge delivery goes the distance. *Science* 2017;356:582-3. DOI PubMed
9. Hamed H, Yari S, D'haen J, et al. Demystifying charge transport limitations in the porous electrodes of lithium-ion batteries. *Adv Energy Mater* 2020;10:2002492. DOI
10. Farid T, Rafiq MI, Ali A, Tang W. Transforming wood as next-generation structural and functional materials for a sustainable future. *EcoMat* 2022;4:e12154. DOI
11. Kim J, Kim Y, Yoo J, Kwon G, Ko Y, Kang K. Organic batteries for a greener rechargeable world. *Nat Rev Mater* 2023;8:54-70. DOI
12. Poizot P, Gaubicher J, Renault S, Dubois L, Liang Y, Yao Y. Opportunities and challenges for organic electrodes in electrochemical energy storage. *Chem Rev* 2020;120:6490-557. DOI PubMed
13. Lee B, Ko Y, Kwon G, et al. Exploiting biological systems: toward eco-friendly and high-efficiency rechargeable batteries. *Joule* 2018;2:61-75. DOI
14. Wang H, Fu F, Huang M, et al. Lignin-based materials for electrochemical energy storage devices. *Nano Mater Sci* 2023;5:141-60. DOI
15. Wang Y, Wang X, Tang J, Tang W. A quinoxalinophenazinedione covalent triazine framework for boosted high-performance aqueous zinc-ion batteries. *J Mater Chem A* 2022;10:13868-75. DOI
16. Wang X, Xiao J, Tang W. Hydroquinone versus pyrocatechol pendants twisted conjugated polymer cathodes for high-performance and robust aqueous zinc-ion batteries. *Adv Funct Mater* 2022;32:2108225. DOI
17. Jia R, He C, Li Q, Liu SY, Liao G. Renewable plant-derived lignin for electrochemical energy systems. *Trends Biotechnol* 2022;40:1425-38. DOI
18. Chen C, Xu S, Kuang Y, et al. Nature-inspired tri-pathway design enabling high-performance flexible Li-$O_2$ batteries. *Adv Energy Mater* 2019;9:1802964. DOI
19. Farid T, Wang Y, Rafiq MI, Ali A, Tang W. Porous flexible wood scaffolds designed for high-performance electrochemical energy storage. *ACS Sustain Chem Eng* 2022;10:7078-90. DOI
20. Zeng Z, Shan X, Hao G, et al. Semiquantitative microscopic pore characterizations of the metamorphic rock reservoir in the central paleo-uplift belt, Songliao Basin. *Sci Rep* 2022;12:2606. DOI PubMed PMC
21. Masara F, Honorio T, Benboudjema F. Sorption in C-S-H at the molecular level: disjoining pressures, effective interactions, hysteresis, and cavitation. *Cement Concrete Res* 2023;164:107047. DOI
22. Thommes M, Cychosz KA. Physical adsorption characterization of nanoporous materials: progress and challenges. *Adsorption* 2014;20:233-50. DOI
23. Shi C, Li X, Yang W, et al. Anchoring ultra-small $Mo_2C$ nanocrystals on honeycomb-structured N-doped carbon spheres for efficient hydrogen evolution. *Chem Commun* 2022;58:5269-72. DOI
24. Sun B, Su Y, Wang X, Chai Y. The influence of vacuum heat treatment on the pore structure of earlywood and latewood of larch. *Holzforschung* 2022;76:985-93. DOI
25. Kojiro K, Miki T, Sugimoto H, Nakajima M, Kanayama K. Micropores and mesopores in the cell wall of dry wood. *J Wood Sci* 2010;56:107-11. DOI
26. Koriem OA, Showman MS, El-shazly AH, Elkady MF. Cellulose acetate/polyvinylidene fluoride based mixed matrix membranes impregnated with UiO-66 nano-MOF for reverse osmosis desalination. *Cellulose* 2023;30:413-26. DOI
27. Halloub A, Raji M, Essabir H, et al. Intelligent food packaging film containing lignin and cellulose nanocrystals for shelf life extension

of food. *Carbohydr Polym* 2022;296:119972. DOI
28. Bui NQ, Fongarland P, Rataboul F, et al. FTIR as a simple tool to quantify unconverted lignin from chars in biomass liquefaction process: application to SC ethanol liquefaction of pine wood. *Fuel Process Technol* 2015;134:378-86. DOI
29. Lin Z, Shi HY, Lin L, Yang X, Wu W, Sun X. A high capacity small molecule quinone cathode for rechargeable aqueous zinc-organic batteries. *Nat Commun* 2021;12:4424. DOI PubMed PMC
30. Bhagia S, Ďurkovič J, Lagaňa R, et al. Nanoscale FTIR and mechanical mapping of plant cell walls for understanding biomass deconstruction. *ACS Sustain Chem Eng* 2022;10:3016-26. DOI
31. Sahoo BP, Das D, Rath P, Chakrabarty S, Roy S, Mohanta K. Improving reinforcement properties of CNTs in aluminium matrix composites: a case of surface modification through AlN nano-particle grafting. *Surf Interfaces* 2023;36:102571. DOI
32. Zhang D, Zhang X, Chen Y, Yu P, Wang C, Ma Y. Enhanced capacitance and rate capability of graphene/polypyrrole composite as electrode material for supercapacitors. *J Power Sources* 2011;196:5990-6. DOI
33. Wu W, Yang L, Chen S, et al. Core-shell nanospherical polypyrrole/graphene oxide composites for high performance supercapacitors. *RSC Adv* 2015;5:91645-53. DOI
34. Duan Z, Hu M, Jiang S, Du G, Zhou X, Li T. Cocuring of epoxidized soybean oil-based wood adhesives and the enhanced bonding performance by plasma treatment of wood surfaces. *ACS Sustain Chem Eng* 2022;10:3363-72. DOI
35. Dong Y, Gao S, Wang K, et al. The effect mechanism and properties of poplar wood cross-linking modified with polyols and polycarboxylic acid. *Wood Mater Sci Eng* 2023;18:1630-40. DOI
36. Li S, Zhang L, Zhang L, et al. The *in situ* construction of three-dimensional core-shell-structured $TiO_2$@PPy/rGO nanocomposites for improved supercapacitor electrode performance. *New J Chem* 2021;45:1092-9. DOI
37. Lei Y, Huo D, Liu H, et al. An investigation of PPy@1T/2H $MoS_2$ composites with durable photothermal-promoted effect in photo-fenton degradation of methylene blue and in water evaporation. *Polymers* 2023;15:3900. DOI PubMed PMC
38. Liu Z, Sun J, Song H, et al. High performance polypyrrole/SWCNTs composite film as a promising organic thermoelectric material. *RSC Adv* 2021;11:17704-9. DOI PubMed PMC
39. López-García F, Canché-Escamilla G, Ocampo-Flores AL, Roquero-Tejeda P, Ordóñez LC. Controlled size nano-polypyrrole synthetized in micro-emulsions as pt support for the ethanol electro-oxidation reaction. *Int J Electrochem Sci* 2013;8:3794-813. DOI
40. Kasisomayajula SV, Qi X, Vetter C, Croes K, Pavlacky D, Gelling VJ. A structural and morphological comparative study between chemically synthesized and photopolymerized poly(pyrrole). *J Coat Technol Res* 2010;7:145-58. DOI
41. Farea MA, Mohammed HY, sayyad PW, et al. Carbon monoxide sensor based on polypyrrole-graphene oxide composite: a cost-effective approach. *Appl Phys A* 2021;127:681. DOI
42. Kumar D, Ail U, Wu Z, et al. Zinc salt in "water-in-polymer salt electrolyte" for zinc-lignin batteries: electroactivity of the lignin cathode. *Adv Sustain Syst* 2023;7:2200433. DOI
43. Wang D, Yang F, Cong L, et al. Lignin-containing hydrogel matrices with enhanced adhesion and toughness for all-hydrogel supercapacitors. *Chem Eng J* 2022;450:138025. DOI
44. Wang M, Wang G, Naisa C, et al. Poly(benzimidazobenzophenanthroline)-ladder-type two-dimensional conjugated covalent organic framework for fast proton storage. *Angew Chem Int Ed* 2023;62:e202310937. DOI
45. Liu L, Solin N, Inganäs O. Bio based batteries. *Adv Energy Mater* 2021;11:2003713. DOI
46. Mei B, Munteshari O, Lau J, Dunn B, Pilon L. Physical interpretations of nyquist plots for EDLC electrodes and devices. *J Phys Chem C* 2018;122:194-206. DOI
47. Wang Y, Lin X, Liu T, et al. Wood-derived hierarchically porous electrodes for high-performance all-solid-state supercapacitors. *Adv Funct Mater* 2018;28:1806207. DOI
48. Tang Z, Pei Z, Wang Z, et al. Highly anisotropic, multichannel wood carbon with optimized heteroatom doping for supercapacitor and oxygen reduction reaction. *Carbon* 2018;130:532-43. DOI
49. Zhang S, Wu C, Wu W, et al. High performance flexible supercapacitors based on porous wood carbon slices derived from Chinese fir wood scraps. *J Power Sources* 2019;424:1-7. DOI
50. Zhu C, Liu T, Qian F, et al. Supercapacitors based on three-dimensional hierarchical graphene aerogels with periodic macropores. *Nano Lett* 2016;16:3448-56. DOI
51. Liu K, Mo R, Dong W, Zhao W, Huang F. Nature-derived, structure and function integrated ultra-thick carbon electrode for high-performance supercapacitors. *J Mater Chem A* 2020;8:20072-81. DOI
52. Xiao K, Ding LX, Liu G, Chen H, Wang S, Wang H. Freestanding, hydrophilic nitrogen-doped carbon foams for highly compressible all solid-state supercapacitors. *Adv Mater* 2016;28:5997-6002. DOI
53. Gao T, Zhou Z, Yu J, et al. 3D printing of tunable energy storage devices with both high areal and volumetric energy densities. *Adv Energy Mater* 2019;9:1802578. DOI
54. Cuña A, Tancredi N, Bussi J, et al. Biocarbon monoliths as supercapacitor electrodes: influence of wood anisotropy on their electrical and electrochemical properties. *J Electrochem Soc* 2014;161:A1806-11. DOI